Accurate Mode-Separated Energy Release Rates for Delamination Cracks

Hae-Soo Oh† [1]

Dept. of Mathematics, University of North Carolina at Charlotte, Charlotte, NC 28223-0001

E-mail: hso@uncc.edu

Key Words: Method of Auxiliary Mapping, the p-Version of the Finite Element Method, Mode-separated Energy Release Rate Interlaminar Cracks, Quarter-Point Singularity Elements .

Following Irwin's argument, the energy release rates are computed by using nodal forces a head of the crack front and relative displacements behind the crack front. Furthermore, the quarter-point singularity elements were used for most finite element computations. Recently, Babuska and Oh introduced a new approach, called the method of auxiliary mapping (MAM), that can effectively handle singularities in the framework of the p-Version of the FEM. In this paper, this new approach is modified so that it can yield highly accurate mode-separated energy release rate for the cracks in composite materials. The results obtained by this method are more accurate than those obtained by the conventional methods. It is known that the mode separated energy release rates for interfacial cracks of bimaterials do not converge. However, we claim that in practical point of view, the mode-separated energy rates of interlaminar cracks of a laminate whose layers are of the same material and may have different fiber orientations converge. Moreover, the total energy release rate will directly computed by differentiating the total strain energy with respect to the crack length.

1. INTRODUCTION

This paper is organized as follows:

• In section 2, the terminologies and notations are introduced.

• In section 3, a new method to obtain highly accurate mode-separated energy release rates is developed.

[1]This research is supported in part by NSF grant INT-9722699.

• In section 4, it is shown that the mode-separated energy release rates for interlaminar cracks of the laminates whose layers are of the same materials virtually converge.

• In section 5, various numerical tests which demonstrate the effectiveness of the method are given.

• In appendix, the proofs of the formulas, introduced in section 3, are given.

2. MODE-SEPARATED ENERGY RELEASE RATE

Consider a crack with area a in a deformable ideally brittle (the plastic deformation is negligible) continuum subjected to arbitrary loading. If the applied load is time independent and the crack grows slowly, then according to the law of conservation of energy we have

$$\frac{\partial W}{\partial a} = \frac{\partial U}{\partial a} + \frac{\partial \Gamma}{\partial a} \tag{2.1}$$

where W is the work performed by the applied loads, U is the elastic strain energy and Γ represents the energy spent in increasing the crack area. If γ represents the energy required to form a unit of new material surface, Equation (2.1) can be written as ([5])

$$G = -\frac{\partial \Pi}{\partial a} = \frac{\partial \Gamma}{\partial a} = 2\gamma, \tag{2}$$

which represents the fracture criterion for the crack growth. Here $\Pi = U - W$ is the potential energy of the system.

If the work of the body force is ignored, Equation (2) takes the form

$$G = -\frac{\partial U}{\partial a}, \tag{3}$$

that is called the **Strain Energy Release Rate.**

Consider the two dimensional case where the crack extends along its own direction in a self-similar manner. Then the central difference approximation (CDA) for the energy release rate is the following.

$$G \approx \frac{U(a+\triangle) - U(a-\triangle)}{2\triangle}. \tag{4}$$

On the other hand, by observing that the work necessary to extend the crack from a to $a+\triangle$ is the same as that necessary to close the crack tip from $a+\triangle$ to a, Irwin ([17], [15]) obtained the energy release rate as

$$\begin{aligned} G &= \lim_{\triangle\to 0} \frac{1}{2\triangle} \int_0^{\triangle} \sigma_y(r,0)[u_y(\triangle - r, \pi) - u_y(\triangle - r, -\pi)]dr \\ &+ \lim_{\triangle\to 0} \frac{1}{2\triangle} \int_0^{\triangle} \tau_{xy}(r,0)[u_x(\triangle - r, \pi) - u_x(\triangle - r, -\pi)]dr, \end{aligned} \tag{5}$$

which is known as the virtual crack closure technique (VCCT). Here u_x and u_y represent the x- and the y- component of the displacement vector, respectively.

Two integrals in this formula are called the opening mode (Mode I) and the sliding mode (Mode II), respectively. They are written as

$$G_I \approx \frac{1}{2\triangle}\int_0^{\triangle} \sigma_y(r,0)[u_y(\triangle - r,\pi) - u_y(\triangle - r,-\pi)]dr, \tag{6}$$

$$G_{II} \approx \frac{1}{2\triangle}\int_0^{\triangle} \tau_{xy}(r,0)[u_x(\triangle - r,\pi) - u_x(\triangle - r,-\pi)]dr. \tag{7}$$

However, for most composite materials, the modes are inseparable. Thus, in this respect, CDA is more accurate then VCCT in the computation of total energy release rates.

In ([27]), the Central Difference Approximation (4) was discarded because (a) the computation involves differences of large numbers divided by a small number and hence the resulting value is not accurate, and (b) this procedure involves two finite element runs. However, in this paper, (4) is employed to estimate the total energy release rate. Moreover, it is shown that CDA Approach (4) is even better than the VCCT Approach in computations of total energy release rates. Actually, unlike the p-version, the CDA approach is not realistic for the h-version of the FEM because it is too expensive to make $\triangle$ sufficiently small.

In applying the VCCT to compute the energy release rate, numerical estimations of G_I and G_{II} obviously depend on the size of $\triangle$. However, if a cracked body consists of homogeneous material, the integrand of the line integral is of the form $\frac{1}{2\triangle}\int_0^{\triangle} \mathcal{O}(\sqrt{\triangle - x}/\sqrt{x})dx$, which is $\int_0^{\pi/2} \mathcal{O}(\cot t)\sin 2t dt$, by the substitution $x = \triangle \sin^2 t$. Hence, the mode-separated energy release rates (6) and (7) are $\triangle$-independent.

On the other hand, if a crack is along the interface of two dissimilar materials, displacement functions and stress tensor are oscillating singular near the crack tip and hence the integrand is of the form $\mathcal{O}([\sqrt{\triangle - x}/\sqrt{x}] \cdot \sin(\varepsilon \log \sqrt{\triangle - x})\cos(\varepsilon \log x))$ where ε is known as the oscillating factor. Because of the oscillating behavior, the mode-separated energy release rates G_I and G_{II} are $\triangle$-dependent and hence the convergence should be determined. Actually, it has been known in the computational mechanics community ([4],[11],[19],[26]) that G_I and G_{II} of bimaterial interface cracks do not converge.

We believe that the mode-separated energy release rates for interfacial cracks of isotropic bimaterials do not converge. However, in this paper, by applying the method of auxiliary mapping (MAM) developed by Babuška and Oh ([**?**]), it is claimed that, in practical point of view, G_I and G_{II} for interfacial cracks of laminates, whose layers are of the same materials, virtually converge.

Conventional methods to compute the energy release rate are to use nodal forces ahead of the crack tip and relative displacements behind the crack tip with quarter point singular elements in the framework of the h-version of FEM. On the other hand, our method is to use MAM (Method of Auxiliary Mapping, a special method to deal with singularities, shown in Appendix) in the framework of the p-version of FEM.

3. A NEW APPROACH TO COMPUTE ENERGY RELEASE RATES

For brevity, we consider G_I in two dimensional case. Let us consider the line integral

$$\frac{1}{2\triangle}\int_0^{\triangle}\sigma_y(x,0)\delta u_y(x-\Delta,0)dx, \tag{3.1}$$

where $\delta u_y(x-\Delta,0)=[u_y(\triangle-r,\pi)-u_y(\triangle-r,-\pi)]$ is the relative displacement. Suppose the stress tensor σ_y and the y-displacement u_y are oscillating singular functions. Then, in order to get accurate energy release rate, we have to overcome the following problems:

- Low accuracy of FE solutions in the presence of the singularities and the poor approximability due to the oscillating factor ε.
- Low accuracy in Numerical Integration of singular functions. The Finite Element solutions of σ_y and δu_y are singular when the singular basis functions are used in FEM.

We are going to deal with these problems by introducing two auxiliary mappings that map the neighborhood Ω_S in the x-y plane into the domain $\hat{\Omega}_S$ in the ξ-η plane. Let us define **the power auxiliary mapping** by

$$\varphi^{\beta}_{pow}(\xi,\eta)=(\hat{r}^{\beta}\cos(\beta\hat{\theta}),\hat{r}^{\beta}\sin(\beta\hat{\theta})), \tag{2}$$

and **the exponential auxiliary mapping** by

$$\varphi^{(\beta_1,\beta_2)}_{exp}(\xi,\eta)=(e^{\beta_1\xi}\cos(\beta_2\eta),e^{\beta_1\xi}\sin(\beta_2\eta)) \tag{3}$$

respectively. Here $(\hat{r},\hat{\theta})$ is the polar coordinates of (ξ,η).$\beta\geq 1$, and β_1 and β_2 are positive real numbers. Those number are called the mapping sizes.

Suppose $\beta=2,\beta_1=2,\beta_2=0.25$, then we have

$$\begin{aligned}\left[r^{1/2}\sin(0.15\log r)\right]\circ\varphi^{2}_{pow} &= \hat{r}\sin(0.3\log\hat{r}),\\ \left[r^{1/2}\sin(0.15\log r)\right]\circ\varphi^{(2,0.25)}_{exp} &= e^{\xi}\sin(0.3\eta).\end{aligned}$$

We clearly see that the transformed functions are much smoother than the original functions.

In order to destroy the log-type singularity, we can take advantage of the exponential auxiliary mapping. However, this map transforms a neighborhood Ω_S of the crack tip onto an infinite domain. On the other hand, if the intensity α of the $r^{\alpha}\sin(\varepsilon\log r)$-type oscillating singularity is unknown, the exponential auxiliary mapping is more advantageous than the power auxiliary mapping. If the intensity of the singularity is known, two auxiliary mapping yields almost the same results [10]. Since it is known that $\alpha=1/2$ for the crack singularity, throughout this paper, we use the power auxiliary mapping.

(A) Special Approach to have accurate economical Finite Element solutions (see Appendix A for details):

Let $\Omega_S = [-h, h] \times [-h, h]$ be the square neighborhood of the crack tip, where h is the layer thickness. For example, discretize Ω_S into eight triangular elements and 16 quadrilateral elements as shown in Fig. 1. Then $(\varphi^2_{pow})^{-1}(\Omega_S) = \hat{\Omega}_S$ consists of eight curved triangular elements and 16 curved quadrilateral elements as shown in the right side of Fig. 1 (Note that the mapped triangular elements have one curved side and the mapped quadrilateral elements have two curved sides).

In this paper, $\Omega^{(*)}_{st}$ stands for either the reference (standard) quadrilateral element $\Omega^{(q)}_{st}$ or the reference (standard) triangular element $\Omega^{(t)}_{st}$. Let E be an element in Ω_S and $\hat{E} = (\varphi^2_{pow})^{-1}(E)$ be the corresponding element in $\hat{\Omega}_S$. Let $\hat{\Psi}^{(blend)}_{\hat{E}}$ be the elemental mapping of blending type from the standard element $\Omega^{(*)}_{st}$ to $\hat{E}$ (see Appendix A for the construction of the elemental mappings $\hat{\Psi}^{(blend)}_{\hat{E}}$). Then the induced singular elemental mapping $\Psi^S_E : \Omega^{(*)}_{st} \to E$, defined by

$$\begin{array}{ccc} E & \xleftarrow{\varphi^2_{pow}} & \hat{E} \\ {\scriptstyle \Psi^S_E}\uparrow & & \uparrow{\scriptstyle \hat{\Psi}^{(blend)}_{\hat{E}}} \\ \Omega^{(*)}_{st} & = & \Omega^{(*)}_{st} \end{array}$$

generates the singular shape functions on E which resemble the crack singularity.

In appendix A, the curved sides of elements in $\hat{\Omega}_S$ are parameterized so that the singular elemental mappings of any curved elements and the conventional polynomial elemental mappings of any regular elements may agree along their common sides. Thus, by assigning

(i) the singular elemental mapping Ψ^S_E to elements E in Ω_S; and

(ii) the conventional elemental mapping Ψ_E to the elements E in $\Omega \backslash \Omega_S$,

we obtain **"exactly and minimally conforming"** [23] finite element space $S^p(\Omega, \mathcal{T}, \mathcal{M})$. This is, $S^p(\Omega, \mathcal{T}, \mathcal{M})$ is a maximal vector space such that its members are continuous and the composition function of its member with the elemental mappings assigned above are polynomial of degree p in the reference elements $\Omega^{(*)}_{st}$. Here $\mathcal{T}$ denotes a specific mesh on the physical domain Ω, p is the polynomial degree uniformly assigned to the elements in $\mathcal{T}$, and $\mathcal{M}$ is the vector of elemental mappings assigned to each element in $\mathcal{T}$ by the rule described above.

Now the FE solution is the projection of the true displacements onto the finite element space $S^p(\Omega, \mathcal{T}, \mathcal{M})$. In other word, the FE solution in $S^p(\Omega, \mathcal{T}, \mathcal{M})$ is the closest one to the true displacements. Since some members of this finite element space closely resemble the the singular displacement vector near the crack tip, the finite element solution in this finite element space is highly accurate.

It is also shown in appendix A that in the actual finite element analysis, this method uses the conventional finite element method to those elements $\hat{E}_k \in \hat{\Omega}_S$ with the transformed bilinear form and the transformed linear functional (the mapped principal of virtual work), instead of constructing the singular basis functions for the local stiffness matrices and local load vectors for those elements in $E_k \in \Omega_S$. Thus, this method requires virtually no extra-cost.

(B) Method of Integration of Singular functions:

Let $\hat{u}$ be the transformed function of u by the power auxiliary mapping φ^2_{pow}. That is, $\hat{u} = u \circ \varphi^2_{pow}$. Then, substitution of $t = \frac{\pi}{4}(\bar{\xi}+1)$ into (A.17) of appendix A.2 yields the following relation:

$$\int_0^{\Delta} \sigma_y(x,0)u_y(\Delta - x, \pi)dx = \frac{\pi}{4}\int_{-1}^{1} \left[F(\frac{\partial \hat{u}_x}{\partial \xi}, \frac{\partial \hat{u}_x}{\partial \eta}, \frac{\partial \hat{u}_y}{\partial \xi}, \frac{\partial \hat{u}_y}{\partial \eta})(\sqrt{\Delta}\sin T, 0)\right] \cdot \left[\hat{u}_y(0, \sqrt{\Delta}\cos T)\right][\sqrt{\Delta}\cos T]d\bar{\xi},$$

where $T = \frac{\pi}{4}(\bar{\xi}+1)$ and $F(\frac{\partial \hat{u}_x}{\partial \xi}, \frac{\partial \hat{u}_x}{\partial \eta}, \frac{\partial \hat{u}_y}{\partial \xi}, \frac{\partial \hat{u}_y}{\partial \eta})$ is defined by (A.11) in appendix A.2. Since $\left[(r^{1/2}\cos\varepsilon \ln r) \circ \varphi^2_{pow}\right](\hat{r}, \hat{\theta}) = \hat{r}\cos 2\varepsilon \ln \hat{r}$, the shifted displacement functions, $\hat{u}_x = u_x \circ \varphi^2_{pow}$ and $\hat{u}_y = u_y \circ \varphi^2_{pow}$, contain no singularities.

Moreover, the FE approximations of $\hat{u}_x$ and $\hat{u}_y$ can be expressed of the form

$$\sum_{l=1}^{m_k} a_l(\phi_l \circ (\hat{\Psi}_k^{(blend)})^{-1})(\xi, \eta),$$

where ϕ_l is a polynomial shape function in the standard element $\Omega_{st}^{(t)}$. For the line integral, $\hat{u}_y$ is evaluate along the straight side $S_2^{(4)} \equiv \overline{6 \to 1}$ of the curved triangular element $\hat{E}_4 \equiv \overline{5 \to 6 \to 1}$ of $\hat{\Omega}_S$ (see Fig. 1) and $\frac{\partial \hat{u}_x}{\partial \xi}, \frac{\partial \hat{u}_x}{\partial \eta}, \frac{\partial \hat{u}_y}{\partial \xi}, \frac{\partial \hat{u}_y}{\partial \eta}$ are evaluated along the straight side $S_3^{(1)} \equiv \overline{1 \to 2}$ of the curved triangular element $\hat{E}_1 \equiv \overline{2 \to 3 \to 1}$ of $\hat{\Omega}_S$ (see Fig. 1).

Since $4L_1L_2$ in (A.9) is vanishing along the side $S_2^{(st)} \equiv \overline{V_2^{(t)} \to V_3^{(t)}}$ and the side $S_3^{(st)} \equiv \overline{V_3^{(t)} \to V_1^{(t)}}$ of $\Omega_{st}^{(t)}$, the element mappings $\hat{\Psi}_1^{(blend)} : \Omega_{st}^{(t)} \longrightarrow \hat{E}_1 \subset \hat{\Omega}_S$ and $\hat{\Psi}_4^{(blend)} : \Omega_{st}^{(t)} \longrightarrow \hat{E}_4 \subset \hat{\Omega}_S$ (Fig. 1) are linear along the sides $S_2^{(st)}$ and $S_3^{(st)}$, respectively. Thus, for this line integral, $(\hat{\Psi}_1^{(blend)})^{-1}$ and $(\hat{\Psi}_4^{(blend)})^{-1}$ are linear and hence $\phi_l \circ \hat{\Psi}_k^{-1}(\xi, \eta), k = 1, 4$ are polynomials. Therefore the Gaussian quadrature of this line integral is almost exact.

On the other hand, because of non-linearity of the blending type elemental mapping $\hat{\Psi}_k^{(blend)} : \Omega_{st}^{(t)} \to \hat{E}_k$, the evaluation of $(\hat{\Psi}_k)^{-1}$ at any interior point of $\hat{E}_k$ requires to use the Newton method. Moreover, $\phi_l \circ (\hat{\Psi}_k^{(blend)})^{-1}$ is no longer polynomial on $\hat{E}_k$. Without using this substitution of integral for the singular functions, a direct numerical integration with respect to a very large number of Gauss points (for example, the interval of integration is divided into ten smaller intervals and apply the Gaussian quadrature with twelve Gauss points on each subinterval) yields similar results to those obtained by the procedure suggested in this section.

(C) The maximum value of the oscillating factor ε is known as 0.17 ([26]). Furthermore, it was shown ([20]) that for most practical orthotropic materials, ε is small. It was showed in ([10]) that MAM yields highly accurate FE solutions of elliptic equations containing oscillating singularities whenever ε is small (for example, $\varepsilon \leq 0.17$).

4. THE CONVERGENCE OF G_I AND G_{II} FOR INTER-LAMINAR CRACKS

Throughout this paper, E and ν denote the modulus of elasticity and Poisson's ratio, respectively. $\lambda = \dfrac{E\nu}{(1+\nu)(1-2\nu)}$ and $\mu = \dfrac{E}{2(1+\nu)}$ are Lame's constants.

Let us consider an interface crack of a bimaterial plate that consists of material 1 with elastic constants μ_1 and ν_1 and material 2 with elastic constants μ_2 and ν_2. Then the oscillating factor, which represents the order of discontinuity of the two materials, is given by

$$\varepsilon = \frac{1}{2\pi} \ln \left[\frac{\mu_1 + \mu_2 \kappa_1}{\mu_2 + \mu_1 \kappa_2} \right], \tag{4.1}$$

where for $i = 1, 2$, $\kappa_i = 3 - 4\nu_i$ for plane strain, $\kappa_i = (3 - \nu_i)/(1 + \nu_i)$ for plane stress.

Without loss of generality, ε may be assumed to be positive and it is zero for a homogeneous plate. Moreover, it takes the maximum value $\ln 3/(2\pi) = 0.17485$ when $\nu_1 = 0$ and $\mu_2 = \infty$. It is known that the mode-separated energy release rates for interface cracks of bimaterials do not converge as $\triangle \to 0$, in general.

Suppose a fiber-reinforced material is a laminate whose layers are of the same material and may have different fiber orientation. Then it can be proved by using similar arguments to those in ([14],[24],[25]) that the oscillating factors of inter-laminar cracks of such laminates are expected to be very small. In other words, the mode-separated energy release rates (6), (7) for such fiber-reinforced materials are virtually constant when

$$10^{-9} \leq \frac{\triangle}{h} \leq 10^{-1}.$$

Moreover, if $\dfrac{\triangle}{h} \leq 10^{-9}$, then $\triangle$ is smaller than the diameter of the fiber and hence the $\triangle$-neighborhood of the crack tip does not contain any fiber. In other words, the $\triangle$-neighborhood of a crack consists of a homogeneous material(resin only) and hence we may claim that $\varepsilon = 0$ whenever $\dfrac{\triangle}{h} \leq 10^{-9}$. Therefore we have the following.

THEOREM 4.1. *The mode-separated energy release rates for the inter-laminar crack of a laminate whose layers are of the same material and may have different fiber orientations virtually converge.*

The computations of the oscillating factors for the delamination cracks of laminates are appeared in a separate paper.

5. COMPUTATIONAL RESULTS

5.1. Cracks in homogeneous materials

Since the displacement functions near crack tip of homogeneous isotropic materials are non-oscillating singular functions, the mode-separated energy release rates converge. In this subsection, the new method presented in section 3 yields better results than the conventional method that use quarter point singularity elements in the framework of the h-version.

It is known that the Mode I energy release rate is expressed in terms of the stress intensity factor K_I as follows:

$$\begin{cases} G_I = \dfrac{K_I^2}{E} & \text{for plane stress,} \\ G_I = \dfrac{(1-\nu^2)K_I^2}{E} & \text{for plane strain,} \end{cases} \tag{5.1}$$

where ν and E are Poisson's ratio and Young's modulus respectively. The expression of G_{II} in terms of K_{II} is similar. In this section, we assume that $\nu = 0.3, E = 10^6$ and the computations are for plain strain.

Example 1. *Center-cracked tension specimen:* We consider a Center-Cracked Plate $[-b, b] \times [-h, h]$ with crack length $2a$ under uniform tension S as shown in Fig. 2(a). Then by appendix 2.1 of [5], the mode I stress intensity factor is

$$K_I = S\sqrt{\pi a}\{1.0 + 0.128(a/b) - 0.288(a/b)^2 + 1.523(a/b)^3\}, \tag{2}$$

when $0 < a/b < 0.7$.

In the first example, we choose $S = 100$, $b = 1.0, a = 0.8, h = 2$. Then by (2) and (5.1), we obtain $G_I = 0.0754556$.

From the symmetries in the problem, only one quarter of the specimen was analyzed. Fig. 2(c) is the p-version finite element mesh which consists of four triangular elements and 15 quadrilateral elements. For the neighborhood of the crack (the mapping zone) for our method, we select the four triangular elements and the four quadrilateral elements that are next to the triangular elements and the specimen was analyzed as follows:

- The mode I energy release rate G_I by the new method.
- The mode I energy release rate $G_{(I)}$ by the conventional p-method without using singularity elements (that is, the mapping size of (A.1) is $\alpha = 1$).
- The total energy release rate by applying Central Difference Approximation to the strain energy computed by the new method.
- The convergence of total strain energy computed by the new method.

Table 1 shows that the relative error of the best $G_I(p = 9)$ is 0.02%. Nevertheless, the best G_I in ([17]), obtained by using cubic singularity elements, has 0.3% in the relative error.

By comparing G_I and $G_{(I)}$ from Table 1, one can see the superiority of the new method over the conventional p-method (that is, 0.02% verses 11% in relative error when $p = 9$). Relative errors in percent of total strain energy, $G_I, G_{(I)}$, and G_{total} are depicted in Fig. 3.

Example 2. *Single Edge-Notched specimen:* The second example is Single edge-notched plate $[-a, b-a] \times [-h, h]$ under uniform tension S as Fig. 2(b). It is known ([5]) that the mode I stress intensity factor for single edge-notched plate is

$$K_I = S\sqrt{\pi a}\{1.12 - 0.23(a/b) + 10.55(a/b)^2 - 21.72(a/b)^3 + 30.39(a/b)^4\}, \tag{3}$$

whenever $0 < a/b < 0.7$.

TABLE 1
Computation of one fourth of Center-Cracked Plate $[-b,b]\times[-h,h]$ with crack length $2a$ under uniform tension $S=100$, where in this computation $b=1.0, a=0.8, h=2$. G_I and $G_{(I)}$ are the mode I energy release rates obtained by the new method and by the conventional p-method respectively. G_{total} is computed by the central difference approximation(4) with $\triangle = 0.5\times 10^{-8}$.

p	DOF	$\mathcal{U}(u_{FE})E/4$	G_I	$G_{(I)}$	G_{total}
1	52	15237.9432999	0.0953976	0.0320149	0.0534118
2	140	16988.7410759	0.0643846	0.0561566	0.0738187
3	236	17078.9934190	0.0719215	0.0577928	0.0753140
4	370	17109.7839910	0.0745717	0.0595203	0.0754432
5	542	17119.5240645	0.0751520	0.0616602	0.0754757
6	752	17121.9398467	0.0752964	0.0633685	0.0754742
7	1000	17122.5523856	0.0753812	0.0648338	0.0754758
8	1286	17122.6845944	0.0754230	0.0660116	0.0754776
9	1610	17122.7069546	0.0754441	0.0669814	0.0754783
∞	∞	17122.7105178	0.0754556	0.0754556	0.0754782

In this example, we use the crack length $a=0.55$ and $b=1.0, h=2.0$, and the remote uniform traction load is $S=100$. Then by (3) and (5.1), we obtain $K_I = 440.6271928$ and $G_I = (1-\nu^2)K_I^2/E = 0.176678$.

Fig. 2(d) is a finite element mesh for the new method which consists of eight triangular elements and 28 quadrilateral elements. For the mapping zone (the neighborhood of the crack tip) for the new method, we select the eight triangular elements and the eight quadrilateral elements that are next to the triangular elements. And the SENS was analyzed in the same ways as the previous example. The results are displayed in Table 2.

Table 2 shows that the relative error of G_I is 0.6% when $p=9$. However, the best G_I in ([17]), obtained by using cubic singularity elements, has 3.3% in the relative error.

By comparing G_I and $G_{(I)}$ from Table 2, once again, one can see the superiority of the new method over the conventional p-method (i.e., 0.6% verses 11.8% in relative error when $p=9$). Relative errors in percent of total energy, $G_I, G_{(I)}$, and G_{total} are depicted in Fig. 4.

5.2. Interfacial Cracks between isotropic layers

In this section, we consider an interface crack of a bimaterial plate that consists of material 1 with elastic constants μ_1 and ν_1 and material 2 with elastic constants μ_2 and ν_2. Then, it is known that the mode-separated energy release rates for interface cracks of bimaterials do not converge as $\triangle \to 0$. Actually, if the oscillating factor ε

TABLE 2
Plain strain Computation for Single edge-notched plate $[-a, b-a] \times [-2, 2]$under uniform tension $S = 100$, where $a = 0.55$ is the crack length and $b = 1.0$. G_I and $G_{(I)}$ are the mode I energy release rates obtained by the new method and by the conventional p-method respectively. G_{total} is computed by the Central Difference Approximation (4) with $\triangle = 0.5 \times 10^{-8}$.

p	DOF	$\mathcal{U}(u_{FE})E$	G_I	$G_{(I)}$	G_{total}
1	80	31156.9824930	0.1502874	0.0555432	0.0979730
2	222	38163.5473336	0.1501532	0.1270484	0.1648749
3	380	38628.4771876	0.1579704	0.1283439	0.1702329
4	602	39122.5168253	0.1721155	0.1378598	0.1747564
5	888	39189.0227303	0.1750825	0.1432396	0.1756045
6	1238	39197.2704305	0.1754222	0.1473620	0.1756870
7	1652	39198.3009764	0.1754423	0.1507687	0.1757009
8	2130	39198.4857040	0.1755709	0.1535316	0.1757021
9	2672	39198.5111936	0.1756254	0.1558046	0.1757029
∞	∞	39198.5156205	0.1766780	0.1766780	0.1766780

is not very small, G_I is increasing (decreasing) while G_{II} is decreasing (increasing), respectively, as $\triangle \to 0$.

Example 3. *Isotropic bimaterial Plate:* Let us consider a bimaterial of epoxy and glass shown in Fig. 5 such that the material properties are as follows:

$$\begin{cases} E_1 = 1.72 \text{ Gpa} \quad \nu_1 = 0.4 \ \text{ (epoxy)}, \\ E_2 = 68.95 \text{ Gpa} \ \ \nu_2 = 0.2 \ \text{ (glass)}. \end{cases} \tag{4}$$

Then from (4.1), $\varepsilon = 0.0486476$. In this example, the sizes of a bimaterial specimen are chosen as follows: the crack length is $a = 0.75dm, a = b, u_0 = 0, v_0 = 6.65\mu m$, and the layer thickness are $h_1 = h_2 = 0.1dm$. The mesh for finite element analysis of this problem is shown as the dotted lines in Fig. 5.

From Fig. 6, one can see that G_I is decreasing and G_{II} is increasing as $\triangle \to 0$. In general, the smaller the oscillating factor ε is, the flatter the curve drawn in $\triangle$ verses G_I/G_{total} (see, [26]). Moreover, it was shown in ([26]) that the graphs of G_I/G_{total} and G_{II}/G_{total} with respect to $\triangle$ are straight lines with small slope when the oscillating factor ε is 0.001.

5.3. Interfacial Cracks between orthotropic layers

In section 5.2, we showed that the mode separated energy rates for interface cracks for isotropic bimaterials do not converge.

In this section, we consider the inter-laminar cracks of laminates of fiber-reinforced layers. If layers are of the same material and may have different fiber directions,

TABLE 3
G_I and G_{II} for interface crack of isotropic bimaterial.

	G_I	G_I	G_{II}	G_{II}
$\triangle/h$	$p=6$	$p=8$	$p=6$	$p=8$
1.0E-1	0.0426679	0.0428116	0.0011769	0.0011675
5.0E-2	0.0415825	0.0416705	0.0023384	0.0023284
5.0E-3	0.0355615	0.0356307	0.0084044	0.0083841
5.0E-4	0.0270981	0.027147	0.0169095	0.0168826
5.0E-5	0.0177138	0.0177394	0.0263338	0.0262994
5.0E-6	0.0090767	0.0090939	0.0349806	0.0349481
1.0E-6	0.0043625	0.0043484	0.0398225	0.0397115

the oscillating factor ε (the order of discontinuity between layers) expected to be very small.

For various tests of inter-laminar cracks of laminates that consist of fiber-reinforced layers with various fiber angles, G_I and G_{II} are virtually constant when $10^{-9} < \triangle/h < 10^{-1}$. Moreover, if $\triangle/h < 10^{-9}$, then the crack tip is well inside the homogeneous materials(resin). In other words, in fiber-reinforced composite materials, if Δ is very small, then physics of the Δ-neighborhood of the material is changed from orthotropic (fiber and resin) to isotropic (resin only). Hence the oscillating factor ε is 0 for such case.

In order to compare our results with the results reported in ([4]), the engineering properties of ply with unidirectional fiber used in examples of this subsection are the same as those in ([4]). That is, material properties of graphite-epoxy ply used in the numerical tests in examples 4(A) and 4(B) are the following.

$$\begin{array}{ll} E_{11} = 19.5 \times 10^6 \text{ psi} & E_{22} = E_{33} = 1.48 \times 10^6 \text{ psi} \\ G_{12} = G_{13} = 0.80 \times 10^6 \text{ psi} & G_{23} = 0.497 \times 10^6 \text{ psi} \\ \nu_{12} = \nu_{13} = 0.30 & \nu_{23} = 0.49 \end{array}$$

Example 4.

(A) The first laminate specimen [0/90/0] consists of plane strain drop-ply configuration of 0° and 90° graphite-epoxy plies as shown in Fig. 7(a), which is Test case # 1 of [4]. In this example, the thickness h of the layer next to the inter-laminar crack is 0.125, the crack length is 0.4, and $\triangle$ denotes the side length of the inner most eight triangular element. The singular zone for our method is the 40 elements inside the square neighborhood $[-0.125, 0.125] \times [-0.125, 0.125]$ of the crack tip.

The new method is applied to estimate G_I and G_{II} when $\triangle/h$ is $10^{-1}, ..., 10^{-7}$. Table 4 is the results when the degree of basis functions are 4, 8, and 9. The results in Table 4 show that the energy release rate is virtually $\triangle$-independent whenever the finite element solution for stress functions are highly accurate (that is, the polynomial degree of basis functions are ≥ 8). On the other hand, if p-degree is ≤ 4, G_I is increasing and G_{II} is decreasing as $\triangle \to 0$. This is a similar pattern as

those reported in ([11]). In order to compare the figures reported in ([4]), G_{II}/G_I verses $\triangle/h$ are plotted in Fig. 9. The results when $p = 4$ is similar to those in [4].

The computation costs are comparable. In this p-version finite element analysis, 90 quadrilateral elements and eight triangular elements are used as it is shown in Fig. 8. On the other hand, in ([4]), 763 eight-noded quadrilateral interpolation elements are used for the finite element analysis of this test problem. The singular and non-singular near-tip meshes consist of 18 rings of elements meshed over a length equal to $h/2$. However, Fig. 8 shows that the near-tip meshes of the new method consist of five rings of elements over $[-h, h] \times [-h, h]$ near the crack tip, $h = 0.125$.

Actually, the new method does not require such a very fine mesh as shown in Fig. 8. If we put only two rings with side length, for example, $r_1 = h/10, r_2 = h/2$, then the number of elements is reduced from 98 to 74 and the mapping zone for the new method consists of eight quadrilateral elements and eight triangular elements. The accuracy of the finite element solution obtained by 74 elements mesh is virtually the same as that obtained by the 98 elements mesh. The reason to put five rings in Fig. 8 is to apply the definition of energy release rate when $\triangle$ is extremely small.

TABLE 4
***G_I* and *G_{II}* for the inter-laminar crack of Drop-ply configuration for the Test #1 of [4] (Fig. 7(a)).**

$\triangle/h$	G_I			G_{II}		
	p = 4	p=8	p=9	p=4	p = 8	p = 9
1.0E-1	2.676E-2	2.723E-2	2.725E-2	0.361E-2	0.396E-2	0.396E-2
1.0E-2	2.678E-2	2.725E-2	2.727E-2	0.359E-2	0.395E-2	0.394E-2
1.0E-3	2.676E-2	2.725E-2	2.727E-2	0.359E-2	0.395E-2	0.394E-2
1.0E-4	2.672E-2	2.725E-2	2.727E-2	0.359E-2	0.395E-2	0.394E-2
1.0E-5	2.646E-2	2.725E-2	2.727E-2	0.377E-2	0.395E-2	0.394E-2
1.0E-6	3.874E-2	2.726E-2	2.727E-2	0.172E-2	0.396E-2	0.394E-2
1.0E-7	3.272E-2	2.726E-2	2.727E-2	0.232E-2	0.396E-2	0.394E-2

(B) Consider a laminate [0/0/90/0] as shown in Fig. 7(b), in which $h = 0.1$. The energy release rates of this case are much higher than those for 4(A) and the mode mix for 4(A) and 4(B) are different as it is pointed out in [4]. This is the Test # 2 of [4].

As shown in Table 5, the mode-separated energy release rates also virtually converge whenever the finite element solutions are highly accurate ($p = 8, 9$). G_{II}/G_I is depicted in Fig. 10 with respect to $\triangle/h = 10^{-n}, n = 1, ..., 7$. Once again, Fig. 10 shows that G_{II}/G_I when $p = 4$ is similar to those in [4].

(C) In the last example, we consider the inter-laminar crack 4(A) (Fig. 7(a)) when the first layer and the second layer are the graphite-epoxy composites and the third layer of 0° fiber orientation is a graphite-polymer composite with the

TABLE 5
G_I and G_{II} for the inter-laminar crack of Drop-ply configuration for the Test # 2 of [4] (Fig. 7(b)) .

$\triangle/h$	G_I			G_{II}		
	p = 4	p=8	p=9	p=4	p = 8	p = 9
1.0E-1	3.310E-2	3.260E-2	3.262E-2	8.526E-2	8.145E-2	8.125E-2
1.0E-2	3.286E-2	3.252E-2	3.254E-2	8.524E-2	8.153E-2	8.133E-2
1.0E-3	3.277E-2	3.252E-2	3.254E-2	8.526E-2	8.152E-2	8.133E-2
1.0E-4	3.306E-2	3.252E-2	3.254E-2	8.647E-2	8.153E-2	8.133E-2
1.0E-5	3.275E-2	3.252E-2	3.254E-2	8.719E-2	8.151E-2	8.132E-2
1.0E-6	2.816E-2	3.252E-2	3.254E-2	8.351E-2	8.154E-2	8.135E-2
1.0E-7	2.990E-2	3.255E-2	3.255E-2	9.343E-2	8.136E-2	8.129E-2

following material properties.

$$E_{11} = 155 \times 10^6 \text{ psi} \qquad E_{22} = E_{33} = 12.10 \times 10^6 \text{ psi}$$
$$G_{12} = G_{13} = 3.20 \times 10^6 \text{ psi} \quad G_{23} = 4.40 \times 10^6 \text{ psi}$$
$$\nu_{12} = \nu_{13} = 0.248 \qquad \nu_{23} = 0.458$$

In this case, the oscillating factor can not be negligible. Thus, as shown in Fig. 11, the mode-separated energy release rates do not converge.

6. CONCLUDING REMARKS

In this paper, we considered only the power auxiliary mapping to deal with the singularities. However, it can not kill the oscillating behavior of the solutions even if it can remove the monotone singularity of type r^λ. On the other hand, the exponential auxiliary mapping is able to remove the log- type singularity as well as the power type (r^λ) singularity from the function containing $r^\lambda sin(\varepsilon \log r)$ type singularity. However, the exponential auxiliary mapping transform a bounded domain into unbounded domain. By using the argument to treat infinite domains in [3], we can take advantage of the exponential auxiliary mapping to have more accurate finite element analysis.

Acknowledgment

The author would like to thank Drs. K. O'Brien and I. Raju for inviting him to NASA Langley Research Center for this research. The author also would like to thank Prof. L. Carlsson for personal correspondence related to this research and encouragement.

APPENDIX

A.1. THE METHOD OF AUXILIARY MAPPING

Babuška and Oh ([3],[12],[13]) introduced a new method, called the Method of Auxiliary Mapping (MAM), that can effectively handle the r^α-type ($\alpha < 1$) singularities [9].

The essence of this method involves locally transforming a neighborhood Ω_S of each singularity point to a new domain $\tilde{\Omega}_S$ by use of the mappings such as $z = \zeta^\beta$ (the power auxiliary mapping) and $z = e^{\beta_1\xi + i\beta_2\eta}$ (the exponential auxiliary mapping), where $z = x + iy, \zeta = \xi + i\eta$. In this paper, we only consider the power auxiliary mapping.

Here β is directly determined by the known nature of the singularity in such a way as to locally transform the exact (singular) solution to a smoother function, which can be easily approximated in the new mapped domain by the conventional use of the p-version of the FEM. In practice, the mapping size β is recommended to be slightly larger than $1/\alpha$ for the power auxiliary mapping. For example, consider a crack singularity of the form $r^{1/2}f(r,\theta)$ located at the origin, where f is smooth. Then the auxiliary mapping $\psi(z) = z^{1/4}$ maps the upper half plane into one half of the first quadrant, and a point $(\hat{r}, \hat{\theta})$ in the lower half of the first quadrant evaluates as $\hat{r}^2 f(\hat{r}^4, 4\hat{\theta})$, a smooth function.

To further understand the effect of the power auxiliary mapping $\psi(z) = z^{1/4}$, let $\Omega_S = \{(r,\theta) : r < R_1, 0 \le \theta \le \pi/4\}$. Then $\hat{\Omega}_S = \psi(\Omega_S) = \{\hat{r}, \hat{\theta}) : \hat{r} \le R_1^{1/4}, 0 \le \hat{\theta} \le \pi/16\}$. If we consider the basis function of p-degree 12 over $\hat{\Omega}_S$, the singular functions created over Ω_S through the power auxiliary mapping restricted to the positive x-axis are generated by $\{1, x^{1/4}, x^{1/2}, x^{3/4}, x, x^{5/4}, ..., x^{11/4}, x^3\}$. That is, the auxiliary mapping implicitly creates special singular basis functions which mimic the singularity.

A.1.1. The Power Auxiliary Mapping and the Model Problem

Let $\varphi^\beta_{pow}(\xi,\eta)$ is a conformal mapping from the ξ-η plane to the x-y plane defined by

$$\varphi^\beta_{pow}(\xi,\eta) = (\hat{r}^\beta \cos(\beta\hat{\theta}), \hat{r}^\beta \sin(\beta\hat{\theta})), \tag{A.1}$$

where $(\hat{r}, \hat{\theta})$ is the polar coordinates of (ξ,η) and the real number $\beta \ge 1$ is called the mapping size.

In order to make the line integral of singular functions in section 3 simple, we use the mapping with mapping size $\beta = 2$. However, our method with mapping size $\beta = 4$ yields a slightly better convergence of the displacement vector.

For brevity, MAM is considered for the following variational equation: Find an element $u \in H^1_0(\Omega) = \{w : \int_\Omega [w^2 + \nabla_x w \cdot \nabla_x w] dxdy < \infty, w = 0 \text{ along } \partial\Omega\}$, which satisfies

$$\mathcal{B}(u,v) = \mathcal{F}(v), \qquad \text{for any } v \in H^1_0(\Omega), \tag{A.2}$$

where

$$\mathcal{B}(u,v) \;=\; \int_\Omega (\nabla_x v)[a_{ij}](\nabla_x u)^T d\Omega, \tag{A.3}$$

$$\mathcal{F}(v) \;=\; \int_{\Omega} f v d\Omega. \tag{A.4}$$

Here $\nabla_x = (\frac{\partial}{\partial x_1}, \frac{\partial}{\partial x_2}) \equiv (\frac{\partial}{\partial x}, \frac{\partial}{\partial y})$. The corresponding forms for the displacement vector can be found in [13].

A.1.2. The Transformed Principal of Virtual Work by the Power Auxiliary Mapping

LEMMA A.1. Let u, v be continuous functions whose derivatives are square integrable, then by the power auxiliary mapping φ^{β}_{pow}, the bilinear form A.3 and the linear functional A.4, are transformed to the following forms:

$$\begin{aligned}\mathcal{B}(u,v) \;\equiv\; & \int_{\Omega_S} (\nabla_x u) \begin{bmatrix} a_{11} & a_{12} \\ a_{21} & a_{22} \end{bmatrix} (\nabla_x v)^T dxdy = \\ & \int_{\hat{\Omega}_S} (\nabla_\xi \hat{u}) \begin{bmatrix} q_{11} & q_{12} \\ q_{21} & q_{22} \end{bmatrix} (\nabla_\xi \hat{v})^T d\xi d\eta \equiv \hat{\mathcal{B}}(\hat{u}, \hat{v}),\end{aligned} \tag{A.5}$$

where

$$\begin{cases} t = & (1-\beta)\hat{\theta} \\ q_{11} = & a_{11}\cos^2 t + a_{22}\sin^2 t - (a_{21}+a_{12})\sin t\cos t \\ q_{12} = & (a_{11}-a_{22})\sin t\cos t - a_{21}\sin^2 t + a_{12}\cos^2 t \\ q_{21} = & (a_{11}-a_{22})\sin t\cos t - a_{12}\sin^2 t + a_{21}\cos^2 t \\ q_{22} = & a_{11}\sin^2 t + a_{22}\cos^2 t + (a_{12}+a_{21})\sin t\cos t. \end{cases}$$

For a continuous function v which is square integrable and an integrable function f, we have

$$\begin{aligned}\mathcal{F}(v) \;\equiv\; & \int_{\Omega_S} f(x,y)v(x,y)dxdy \\ = \; & \int_{\hat{\Omega}_S} \beta^2(\xi^2+\eta^2)^{\beta-1}\hat{f}(\xi,\eta)\hat{v}(\xi,\eta)d\xi d\eta \equiv \hat{\mathcal{F}}(\hat{v}).\end{aligned}$$

A.1.3. Construction of Singular Elemental Mappings

Let $\Omega^{(t)}_{st}$ be the standard triangular element in the ξ_t-η_t plane with vertices $V^{(t)}_1 = (-1,0), V^{(t)}_2 = (1,0), V^{(t)}_3 = (0,\sqrt{3})$. Then

$$\begin{cases} L_1 = (1-\xi_t-\eta_t/\sqrt{3})/2, \\ L_2 = (1+\xi_t-\eta_t/\sqrt{3})/2, \\ L_3 = \eta_t/\sqrt{3}, \end{cases}$$

are the nodal basis functions on $\Omega^{(t)}_{st}$ and represent the area coordinates of $(\xi_t, \eta_t) \in \Omega^{(t)}_{st}$.

Let $\Omega_{st}^{(q)}$ be the standard quadrilateral element in the ξ_t-η_t plane with vertices $V_1^{(q)} = (-1,-1), V_2^{(q)} = (1,-1), V_3^{(q)} = (1,1), V_4^{(q)} = (-1,1)$. Then

$$\begin{cases} N_1 = (1-\xi)(1-\eta)/4, \\ N_2 = (1+\xi)(1-\eta)/4, \\ N_3 = (1+\xi)(1+\eta)/4, \\ N_4 = (1-\xi)(1+\eta)/4 \end{cases}$$

are the nodal basis functions on $\Omega_{st}^{(q)}$.

A1. Parameterization of the curved sides in Fig. 1:

Let $(X_1, Y_1) = (0,0), (X_2, Y_2), (X_3, Y_3), ..., (X_n, Y_n)$ be the coordinates of the nodes $1, 2, 3, ..., n$ of the mesh of Ω_S in Fig. 1, respectively. The coordinates of the corresponding points in $\hat{\Omega}_S$ are denoted by $(\hat{X}_k, \hat{Y}_k), k = 1, 2, ..., n$ (that is, $\varphi_{pow}^2(\hat{X}_k, \hat{Y}_k) = (X_k, Y_k)$). Then, for example, the curved side $\hat{S}_1^{(1)} \equiv \overline{2 \to 3}$, of the curved triangle $\hat{E}_1 \equiv \overline{2 \to 3 \to 1}$, is parameterized as follows:

$$(x_1^{(1)}, y_1^{(1)})(\xi_t) = (\varphi_{pow}^{-2})(\frac{1-\xi_t}{2} X_2 + \frac{1+\xi_t}{2} X_3, \frac{1-\xi_t}{2} Y_2 + \frac{1+\xi_t}{2} Y_3), \quad \text{(A.6)}$$

where $-1 \le \xi_t \le 1$ and $\varphi_{pow}^{-2} = (\varphi_{pow}^2)^{-1}$.

Suppose $\hat{E}_9 \equiv \overline{3 \to 2 \to 11 \to 12}$ is the curved quadrilateral element with two curved sides in Fig. 1. Then, for example, the two curved sides $\hat{S}_1^{(9)} \equiv \overline{3 \to 2}$ and $\hat{S}_3^{(9)} \equiv \overline{11 \to 12}$ are, respectively, parameterized as follows:

$$(x_1^{(9)}, y_1^{(9)})(\xi_t) = \varphi_{pow}^{-2}(\frac{1-\xi_t}{2} X_3 + \frac{1+\xi_t}{2} X_2, \frac{1-\xi_t}{2} Y_3 + \frac{1+\xi_t}{2} Y_2), \quad \text{(A.7)}$$

$$(x_3^{(9)}, y_3^{(9)})(\xi_t) = \varphi_{pow}^{-2}(\frac{1+\xi_t}{2} X_{11} + \frac{1-\xi_t}{2} X_{12}, \frac{1+\xi_t}{2} Y_{11} + \frac{1-\xi_t}{2} Y_{12}), \quad \text{(A.8)}$$

where $-1 \le \xi_t \le 1$.

A2. Elemental Mapping of Blending Type: For example, for the curved triangular element $\hat{E}_1 = (\varphi_{pow}^2)^{-1}(E_1)$ of $\hat{\Omega}_S$ in Fig. 1, the elemental mapping $\hat{\Psi}_1^{(blend)} : \Omega_{st}^{(t)} \longrightarrow \hat{E}_1$, of blending type, is defined as follows:

$$\begin{cases} \Psi_{11} = L_1\hat{X}_2 + L_2\hat{X}_3 + L_3\hat{X}_1 + \dfrac{4L_1L_2}{1-\xi_t}\left[x_1^{(1)}(\xi_t) - (\dfrac{1-\xi_t}{2}\hat{X}_2 + \dfrac{1+\xi_t}{2}\hat{X}_3)\right] \\ \Psi_{12} = L_1\hat{Y}_2 + L_2\hat{Y}_3 + L_3\hat{Y}_1 + \dfrac{4L_1L_2}{1-\xi_t}\left[y_1^{(1)}(\xi_t) - (\dfrac{1-\xi_t}{2}\hat{Y}_2 + \dfrac{1+\xi_t}{2}\hat{Y}_3)\right]. \end{cases} \quad \text{(A.9)}$$

The blending type elemental mapping $\hat{\Psi}_9$ from $\Omega_{st}^{(q)}$ onto the curved quadrilateral element $\hat{E}_9 \subset \hat{\Omega}_S$ with two curved sides $\hat{S}_1^{(9)}$ and $\hat{S}_3^{(9)}$ are constructed in a similar manner by using (A.6) and (A.7) (see, chapter 6 of [23]).

A3. Singular Elemental Mapping: Let us define an elemental mapping from $\Omega_{st}^{(*)}$ onto $E_k \subset \Omega_S$ by

$$\Psi_k^S(\xi_t, \eta_t) = [\varphi_{pow}^2 \circ \hat{\Psi}_k^{(blend)}](\xi_t, \eta_t).$$

Then for a standard shape functions ϕ_j on $\Omega_{st}^{(*)}$, $\phi_j \circ (\Psi_k^S)^{-1}$ is a singular shape function on E_k, which is of $r^{1/2}$-type.

A.1.4. Construction of the Finite Element Spaces

Suppose $\mathcal{T} = \{E_k : k = 1, ..., N(\mathcal{T})\}$ represents a specific mesh on Ω. Let $\mathcal{M} = \{\Psi_k^S, k = 1, ..., n\} \cup \{\Psi_k, k = n+1, ..., N(\mathcal{T})\}$ be the vector of element mappings assigned to each element in $\mathcal{T}$ in the following way:

(1) Assign the standard polynomial elemental mappings Ψ_k to the elements E_k in $\Omega \backslash \Omega_S$.
(2) Assign the singular elemental mappings Ψ_k^S to the elements E_k in Ω_S.

Let $\mathcal{P}_p(\Omega_{st}^{(*)})$ be the space of polynomials of degree p defined on $\Omega_{st}^{(*)}$. Then the finite element space $S^p(\Omega, \mathcal{T}, \mathcal{M})$ is the space of all continuous functions u defined on Ω such that

1. The strain energy of u is finite.
2. $u \circ \Psi_k^S \in \mathcal{P}_p(\Omega_{st}^{(*)})$ for each $E_k \subseteq \Omega_S$ (Ψ_k^S is the singular elemental mapping).
3. $u \circ \Psi_k \in \mathcal{P}_p(\Omega_{st}^{(*)})$ for each $E_k \subseteq \Omega \backslash \Omega_S$ (Ψ_k is the regular polynomial elemental mapping).

The Finite element solution u_{FE} is the function that is in the finite element space $S^p(\Omega, \mathcal{T}, \mathcal{M})$ and is the closest among the functions in the finite element space to the exact solution.

The dimension of the vector space $S^p(\Omega, \mathcal{T}, \mathcal{M})$ is called the **Number of Degree of Freedom.** Let us note that in **the p-version of FEM** the mesh $\mathcal{T}$ of the domain is fixed and only the degree p of the basis polynomials is increased to obtain the desired accuracy.

It could be a lot of extra work to construct the singular basis functions constructed through the above mapping technique for the local stiffness matrices and local load vectors. However, the novelty of our method is avoiding this extra work as follows: instead of construing the singular basis functions in $S^p(\Omega, \mathcal{T}, \mathcal{M})$, we use the transformed bilinear form $\hat{\mathcal{B}}(\cdot, \cdot)$ and $\hat{\mathcal{F}}(\cdot)$ (the right side integrals in Lemme A.1), which is the conventional FEM to compute local stiffness matrices and local load vectors for the corresponding curved elements $\hat{E}$. Thus, the proposed method requires virtually not more extra work than the conventional FEM.

A.2. LINE INTEGRAL

With respect to the power auxiliary mapping $\varphi_{pow}^2(\xi, \eta)$ with the mapping size 2, we have

$$\begin{aligned} dx &= \frac{dx}{d\xi} d\xi + \frac{dx}{d\eta} = J_{11} d\xi + J_{12} d\eta \\ dy &= \frac{dy}{d\xi} d\xi + \frac{dy}{d\eta} = J_{21} d\xi + J_{22} d\eta, \end{aligned}$$

where

$$\begin{aligned} J_{11} &= 2\hat{r}\cos\hat{\theta} \quad J_{12} = 2\hat{r}\sin\hat{\theta} \\ J_{21} &= -2\hat{r}\sin\hat{\theta} \quad J_{22} = 2\hat{r}\cos\hat{\theta}. \end{aligned}$$

Furthermore, if we let $\hat{v}(\xi,\eta) = v \circ \varphi^2_{pow}(\xi,\eta)$, then we have

$$\left\{\frac{\partial v}{\partial x}, \frac{\partial v}{\partial y}\right\}^T = [J_{ij}]^{-1} \cdot \left\{\frac{\partial \hat{v}}{\partial \xi}, \frac{\partial \hat{v}}{\partial \eta}\right\}^T \tag{A.10}$$

where

$$[J_{ij}]^{-1} = \frac{1}{2\hat{r}} \begin{bmatrix} \cos\hat{\theta} & -\sin\hat{\theta} \\ \sin\hat{\theta} & \cos\hat{\theta} \end{bmatrix}. \tag{A.11}$$

We denote the displacement vector $\{u\}$ and represent it as 2×1 matrix:

$$\{u\} = \{u_x(x,y), u_y(x,y)\}^T.$$

The corresponding strain tensor and stress tensor are represented by $\{\varepsilon\} = \{\frac{\partial u_x}{\partial x}, \frac{\partial u_y}{\partial y}, \frac{\partial u_x}{\partial y} + \frac{\partial u_y}{\partial x}\}^T$ and $\{\sigma\} = \{\sigma_x, \sigma_y, \tau_{xy}\}^T$. We denote the stress-strain relationships as follows:

$$\{\sigma\} = [E_{ij}]\{\varepsilon\}.$$

Then we obtain

$$\begin{aligned} \hat{\sigma}_y(\xi,\eta) &= \sigma \circ \varphi^2_{pow}(\xi,\eta) \\ &= \frac{1}{2\hat{r}} \Big[(E_{21}\cos\hat{\theta} + E_{23}\sin\hat{\theta}) \frac{\partial \hat{u}_x}{\partial \xi} + (-E_{21}\sin\hat{\theta} + E_{23}\cos\hat{\theta}) \frac{\partial \hat{u}_x}{\partial \eta} \\ &+ (E_{22}\sin\hat{\theta} + E_{23}\cos\hat{\theta}) \frac{\partial \hat{u}_y}{\partial \xi} \\ &+ (E_{22}\cos\hat{\theta} - E_{23}\sin\hat{\theta}) \frac{\partial \hat{u}_y}{\partial \eta} \Big] (\xi,\eta) \end{aligned} \tag{A.12}$$

Letting the inside of the square bracket by $F(\frac{\partial \hat{u}_x}{\partial \xi}, \frac{\partial \hat{u}_x}{\partial \eta}, \frac{\partial \hat{u}_y}{\partial \xi}, \frac{\partial \hat{u}_y}{\partial \eta})$, the equation (A.11) can be written as

$$\hat{\sigma}_y(\xi,\eta) = \frac{1}{2\hat{r}} F(\frac{\partial \hat{u}_x}{\partial \xi}, \frac{\partial \hat{u}_x}{\partial \eta}, \frac{\partial \hat{u}_y}{\partial \xi}, \frac{\partial \hat{u}_y}{\partial \eta})(\xi,\eta). \tag{A.13}$$

Since $d\eta = 0$ along the ξ-axis,

$$ds = \sqrt{dx^2 + dy^2} = \sqrt{(J_{11}d\eta)^2 + (J_{12}d\eta)^2} = 2\hat{r}d\xi \tag{A.14}$$

along $\hat{\theta} = 0$.

Let us denote g be a function defined by $g(x,y) = (\triangle - x, y)$, then

$$\begin{aligned} u_y \circ g \circ \varphi^2_{pow}(\hat{r},\hat{\theta}) &= u_y \circ \varphi^2_{pow} \circ (\varphi^2_{pow})^{-1} \circ g \circ \varphi^2_{pow}(\hat{r},\hat{\theta}) \\ &= u_y \circ \varphi^2_{pow} \circ (\varphi^2_{pow})^{-1} \circ g \circ (\hat{r}^2, 2\hat{\theta}) \\ &= \hat{u}_y \circ (\varphi^2_{pow})^{-1} (\triangle - \hat{r}^2, 2\hat{\theta}) \\ &= \hat{u}_y(\sqrt{\triangle - \hat{r}^2}, \hat{\theta}). \end{aligned} \tag{A.15}$$

And also note that through the auxiliary mapping φ^2_{pow}, the lines $\theta = \pi$ and $\theta = -\pi$ are mapped to the line $\hat{\theta} = \pi/2$ and $\hat{\theta} = -\pi/2$, respectively in the ξ-η plane.

Then from (A.11), (A.13), (A.14) and (A.14), we have

$$\begin{aligned}
\int_0^{\Delta} \sigma_y(x,0)u_y(\Delta - r,\pi)ds &= \int_0^{\Delta} \sigma_y(x,0)u_y \circ g(r,\pi)ds \\
&= \int_0^{\sqrt{\triangle}} [\sigma_y \circ \varphi^2_{pow}(\xi,0)][u_y \circ g \circ \varphi^2_{pow}(\xi,\pi/2)]2\hat{r}d\xi \\
&= \int_0^{\sqrt{\triangle}} \hat{\sigma}_y(\xi,0)\hat{u}_y(\sqrt{\triangle - \xi^2},\pi/2)2\hat{r}d\xi \\
&= \int_0^{\sqrt{\triangle}} F(\frac{\partial \hat{u}_x}{\partial \xi},\frac{\partial \hat{u}_x}{\partial \eta},\frac{\partial \hat{u}_y}{\partial \xi},\frac{\partial \hat{u}_y}{\partial \eta})(\xi,0)\hat{u}_y(\sqrt{\triangle - \xi^2},\pi/2)d\xi \\
&= \int_0^{\sqrt{\triangle}} F(\frac{\partial \hat{u}_x}{\partial \xi},\frac{\partial \hat{u}_x}{\partial \eta},\frac{\partial \hat{u}_y}{\partial \xi},\frac{\partial \hat{u}_y}{\partial \eta})(\xi,0)\hat{u}_y(0,\sqrt{\triangle - \xi^2})d\xi \qquad \text{(A.16)}
\end{aligned}$$

By the substitution $\xi = \sqrt{\triangle}\sin t$, the forgoing line integral becomes

$$\int_0^{\pi/2} \left[F(\frac{\partial \hat{u}_x}{\partial \xi},\frac{\partial \hat{u}_x}{\partial \eta},\frac{\partial \hat{u}_y}{\partial \xi},\frac{\partial \hat{u}_y}{\partial \eta})(\sqrt{\Delta}\sin t,0)\right]\left[\hat{u}_y(0,\sqrt{\Delta}\cos t)\right][\sqrt{\Delta}\cos t]d\xi \qquad \text{(A.17)}$$

REFERENCES

1. Anderson, Börje, Urban Falk, Ivo Babuška and Tobias Von Petersdorff: *Reliable Stress and Fracture Mechanics Analysis of Complex Components Using a h-p Version of FEM,* Int J. Numer Meth Eng., Vol. 38, pp2135-2163 (1995).

2. Bakhavalov, N. and G. Panasenko: Homogenization: Averaging Process in Periodic Media, Kluwer Academic Publishers, 1989.

3. Babuška I. and Hae-Soo Oh: *The p-Version of the Finite Element Method for Domains with Corners and for Infinite Domains*, Number. Meth. PDEs., **6**, pp 371-392,(1990).

4. Beuth, J. L. :*Separation of Crack Extension Modes in Orthotropic Delamination Models,* NASA Langley Research Center, NASA Technical Memorandum 109180 (1995), Int. J of Fracture, **77**, pp 305-321 (1996).

5. Gdoutos, E. E.: *Fracture Mechanics: An Introduction,* Kluwer Academic Publishers,1993

6. Guo, B. and H.-S. Oh: *The h-p Version of the Finite Element Method for Problems with Interfaces,* Int. J. for Numerical Methods in Engineering, Vol. 37, p1741-1762 (1994)

7. Herakovich, C.T.: Mechanics of Fibrous Composites, Wiley, 1998.

8. Han, J. and S. V. Hoa: *A Three Dimensional Multilayer Composite Finite Element For Stress Analysis of Composite Laminates,* Int. J. Numer Meth. Eng., Vol. 36, p3903-3914 (1993)

9. Lucas, T.R. and H.-S. Oh: *The Method of Auxiliary Mappings in the Finite Element Solutions of Elliptic Boundary Value Problems Contain ing Boundary or Corner Singularities,* J. of Comp. Physics, **108**, pp327-342 (1993).

10. Oh, Hae-Soo, Hoonjoo Kim, and Sungjin Lee: *The Mapping Techniques in thep Version of the Finite Element Method for Elliptic Boundary Value Problems Containing Oscillating Singularities,* submitted to Comput. Meth Appl. Mech and Eng.

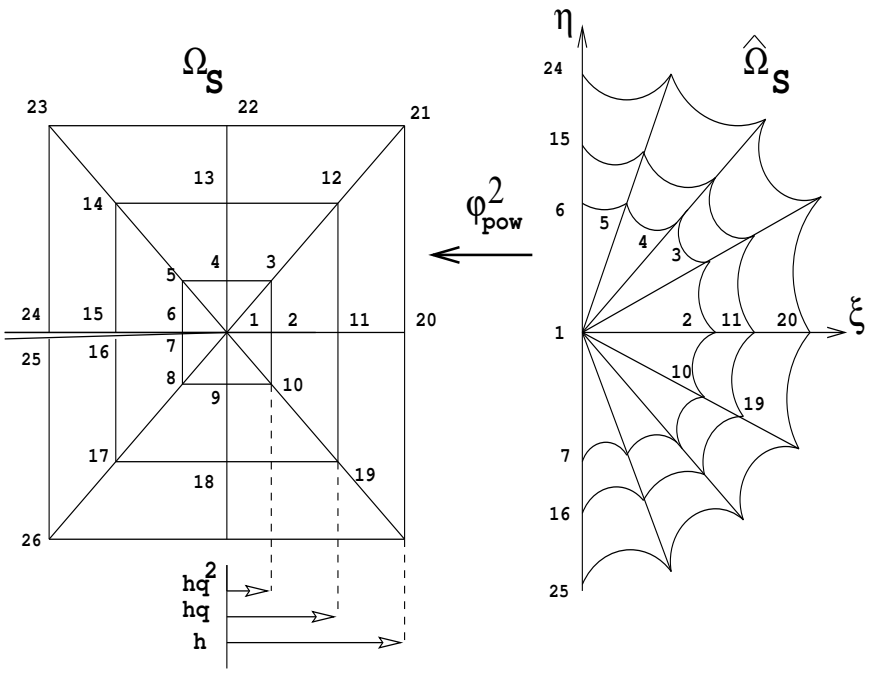

FIG. 1. Scheme of Neighborhood Ω_S of crack tip and the Mapped Neighborhood $\hat{\Omega}_S$.

11. Manoharan, M. G. and Sun, C. T.: *Starin Energy Release Rates of an Interfacial Crack between Two Anisotropic Solids under Uniform Axial Strain,* Composites Science and Technology, Vol. 39, pp99-116 (1990)

12. Oh, H.-S. and Ivo Babuška: *The p-Version of the Finite Element Method for the Elliptic Problems with Interfaces,* Comp. Meth. Appl. Mech. Enrg, **97**, pp211-231 (1992)

13. Oh, H.-S. and Ivo Babuška: *The Method of Auxiliary Mapping For the Finite Element Solutions of Plane Elasticity Problems Containing Singularities,* J. of Computational Physics, **121**, p193-212 (1995)

14. Qu, J. and J. L. Bassani: *Cracks on Bimaterial and Bicrystal Interfaces,* J. Mech. Phys. Solids, **37**, No. 4, pp417-433, 1989.

15. Rybicki, E. F. and Kanninen, M. F.:*A Finite Element Calculation of Stress Intencity Factors by a Modified Crack Closure Integral,* Eng. Fracture Mechanics, Vol. 9 pp 931-938 (1977)

16. Raju, I. S.:*Calculation of Strain Energy Release Rates with Higher Order and Singular Finite Elements,* Engineering Fracure Mechanics, Vol. 28, no. 3, pp254-274 (1987)

17. Raju, I. S.:*Calculation of Strain Energy Release Rates with Higher Order and Singular Finite Elements,* Engineering Fracure Mechanics, Vol. 28, no. 3, pp254-274 (1987)

18. Rice, J. R.:*Elastic Fracture Mechanics Concepts for Interfacial Cracks,* J. of Applied Mechanics, Vol. 98, pp98-103 (1988)

19. Sun, C.T. and M. G. Manoharan : *Starin Energy Release Rates of an Interfacial Crack between Two Orthotropic Solids,* J. of Composite Materials, Vol. 23, pp460-477 (1989)

20. Suo, Z. : *Singularities, interfaces and cracks in dissimilar anisotropic media,* Proc. of the Royal Society of London A427, pp361-364 (1990)

21. Schön, J. and B. Anderson:*Interaction Between a Delamination Crack and a Matrix Crack* , FFA of Sweden, Technical Report 1998-34, Proceedings of The 13th ASC Annual Technical Conference, 1998.

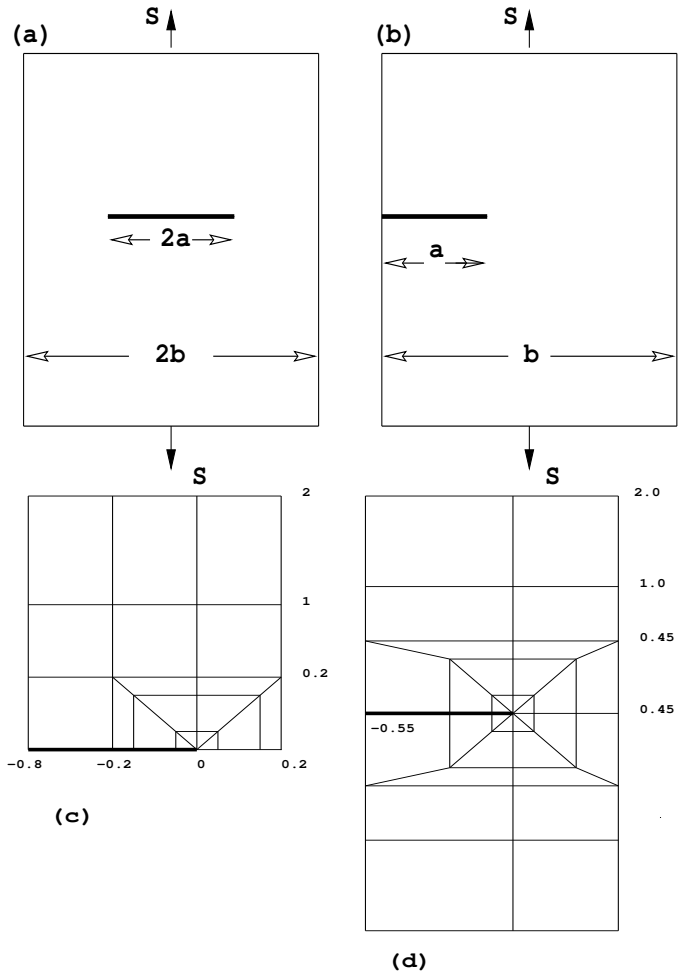

FIG. 2. Schemes of (a) Center Cracked Tension (CCT) specimen, (b) Single Edge Notched (SEN) specimen, (c) Finite Element Mesh of one quarter of CCT specimen, (d) Finite Element Mesh of SEN specimen.

22. Schön, J. and B. Anderson:*Calculation of Mode-Separated Energy Release Rates During Delamination Growth,* FFA of Sweden, Technical Report 1998-27, Proceedings of The 13th ASC Annual Technical Conference, 1998.

23. Szabó, B. and Babuška, I. : Finite Element Analysis, John & Wiley , 1990.

24. Ting, T. C. T.: *Effects of Change of Reference Coordinates on the stress Analyses of Anisotropic Elastic Materials,* Int. J. Solids Structures, **18**, No. 2, pp 139-152, 1982.

25. Ting, T. C. T.: *Explicit Solution and Invariance of the Singularities at an Interface Crack in Antisotropic Composites,* Int. J. Solids Structures, **22**, No. 9, pp 965-983, 1986.

26. Toya, M: *On mode I and mode II energy release rates of an interface crack,* Int. J. of fracture, Vol. 56, pp345-352 (1992)

27. Wang, J. T. and Raju, I. S.:*Strain Energy Release Rate Formula for Skin-Stiffener Debond Modeled with Plate Elements*, Eng. Fracture Mechanics, Vol. 54, No. 2, pp211-228 (1996)

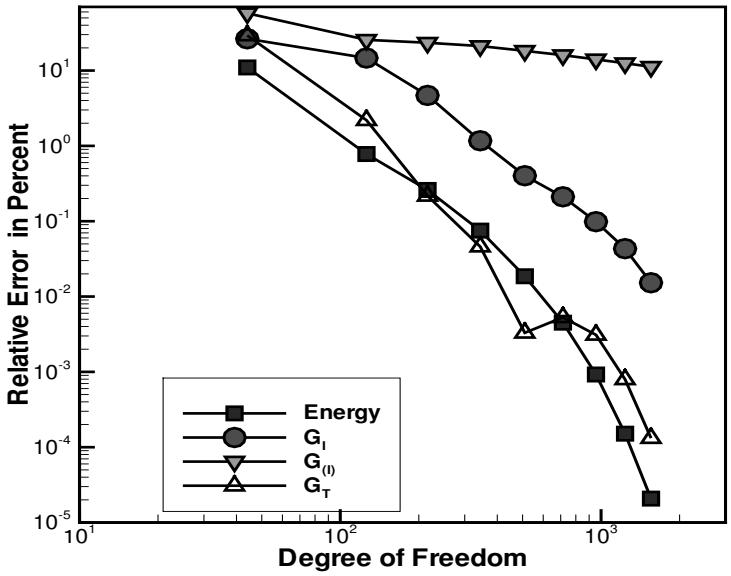

FIG. 3. Relative Error (%) of $G_I, G_{(I)}$(Mode I energy release rate without applying the new method), G_{total} of CCT specimen.

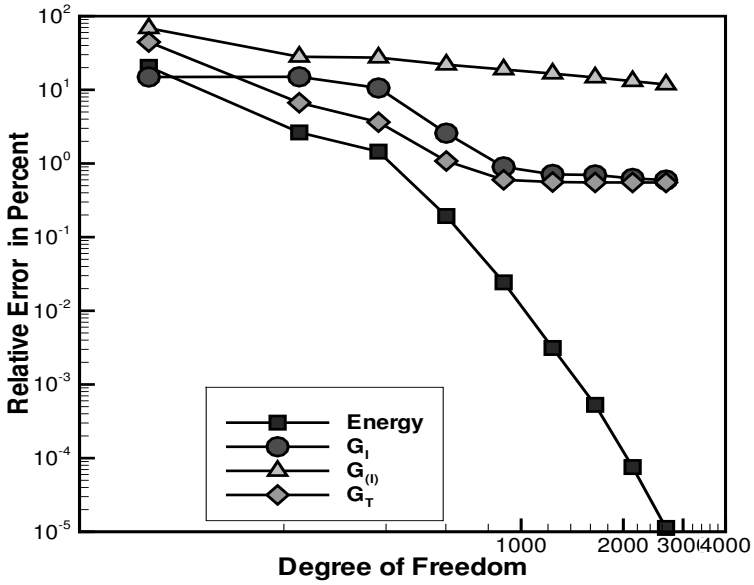

FIG. 4. Relative Error (%) of $G_I, G_{(I)}$(Mode I energy release rate without applying the new method), G_{total} of SEN specimen.

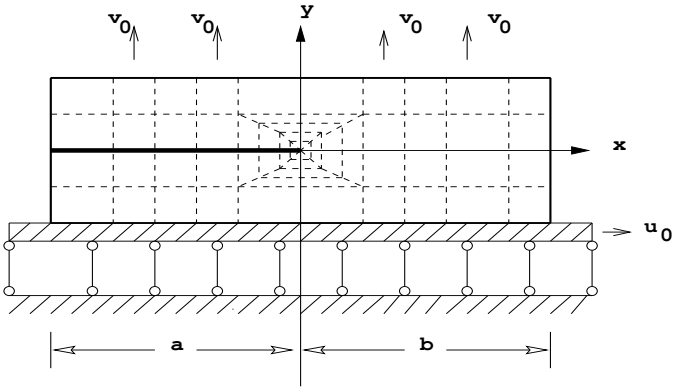

FIG. 5. Scheme of the isotropic bimaterial and Finite Element Mesh (dotted lines)

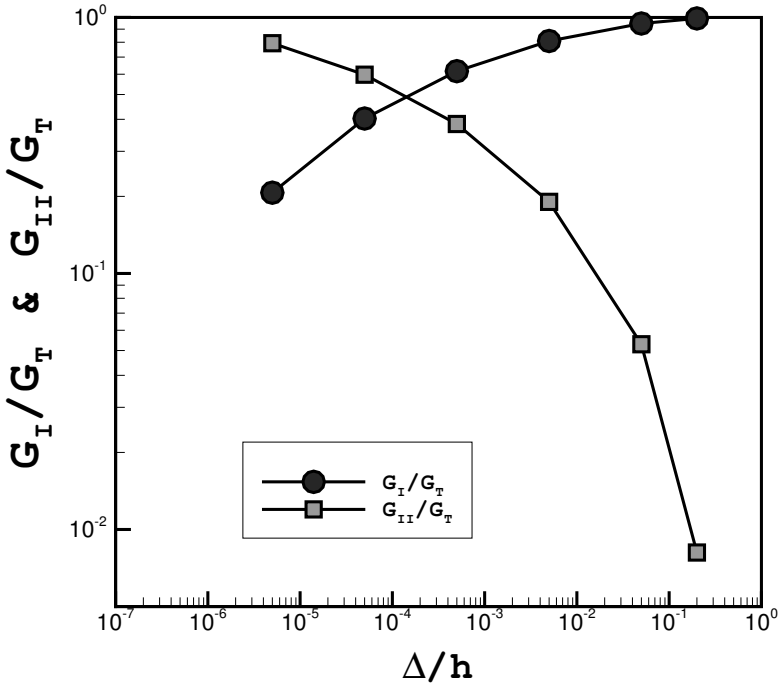

FIG. 6. Finite Element Analysis of G_I and G_{II} for isotropic bimaterial when the oscillating factor $\varepsilon = 0.0486$.

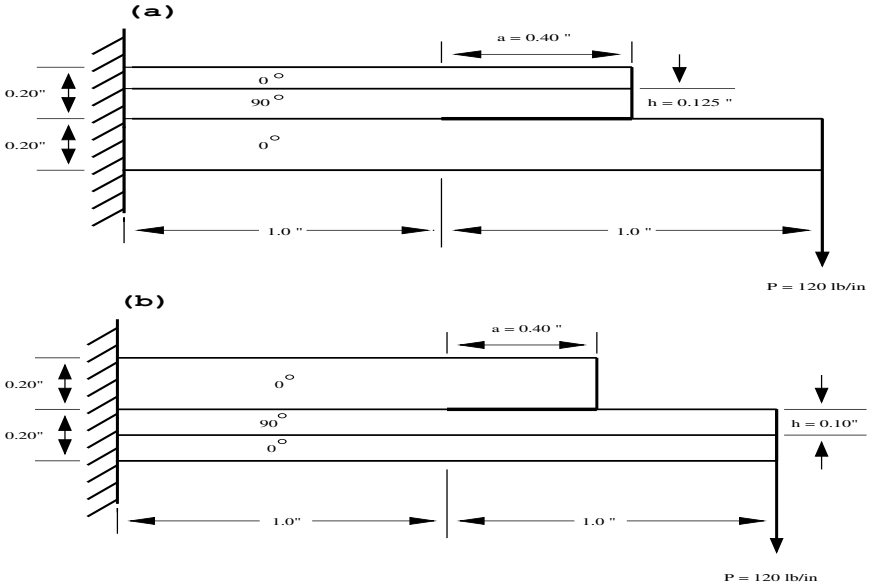

FIG. 7. Scheme of Drop-ply configuration for the Test Problems 4(A) and 4(B).

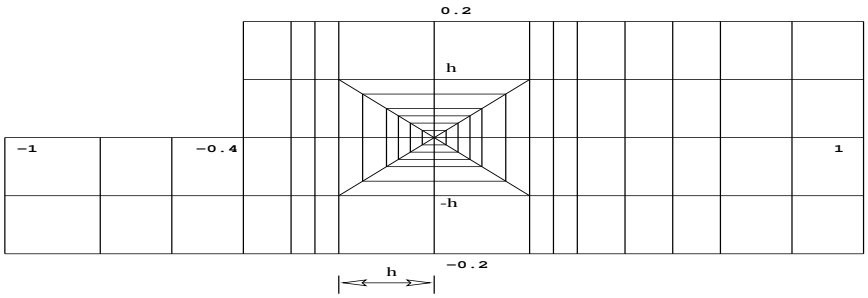

FIG. 8. Mesh for the finite element analysis for the problems 4(A) and 4(B).

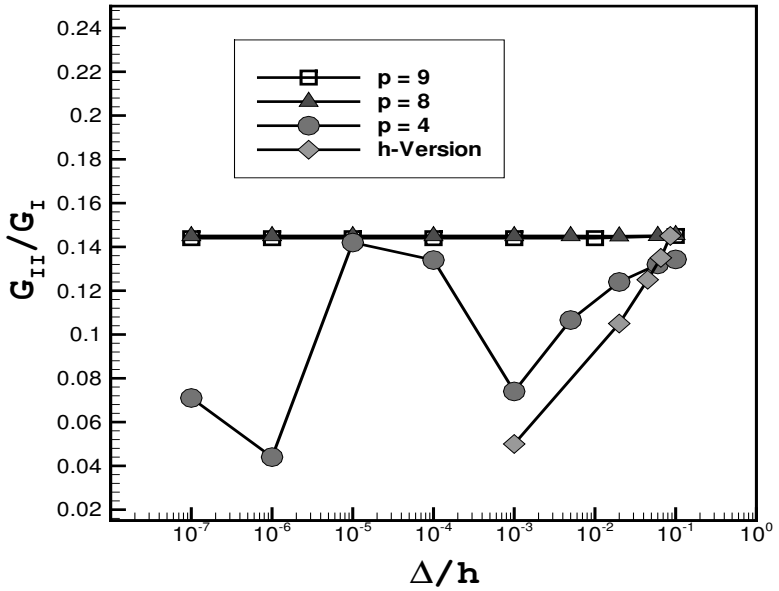

FIG. 9. Results of the p-version finite element analysis of laminate [0/90/0] with $h = 0.125$ (Fig. 7(a)).

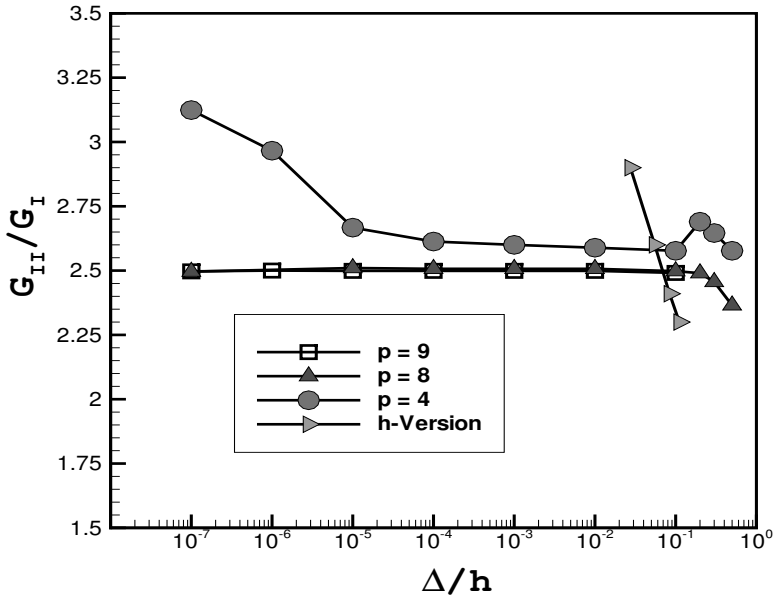

FIG. 10. Results of the p-version finite element analysis of laminate [0/0/90/0] with $h = 0.1$ (Fig. 7(b)).

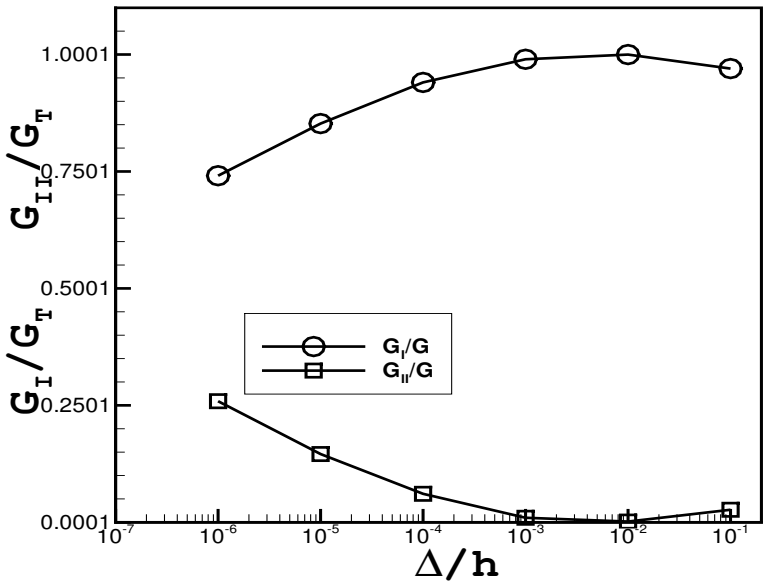

FIG. 11. Results of the *p*-version finite element analysis of the laminate Fig 6(a) when the first two layers are graphite-epoxy composites and the last layer is graphite-polymer composite.